PLANETARY SCIENCE

Thickness and structure of the martian crust from InSight seismic data

Brigitte Knapmeyer-Endrun[1]*, Mark P. Panning[2], Felix Bissig[3], Rakshit Joshi[4], Amir Khan[3,5], Doyeon Kim[6], Vedran Lekić[6], Benoit Tauzin[7,8], Saikiran Tharimena[2]†, Matthieu Plasman[9], Nicolas Compaire[10], Raphael F. Garcia[10], Ludovic Margerin[11], Martin Schimmel[12], Éléonore Stutzmann[9], Nicholas Schmerr[6], Ebru Bozdağ[13], Ana-Catalina Plesa[14], Mark A. Wieczorek[15], Adrien Broquet[16,15], Daniele Antonangeli[17], Scott M. McLennan[18], Henri Samuel[9], Chloé Michaut[19,20], Lu Pan[21], Suzanne E. Smrekar[2], Catherine L. Johnson[22,23], Nienke Brinkman[3], Anna Mittelholz[3], Attilio Rivoldini[24], Paul M. Davis[25], Philippe Lognonné[9,20], Baptiste Pinot[10], John-Robert Scholz[4], Simon Stähler[3], Martin Knapmeyer[14], Martin van Driel[3], Domenico Giardini[3], W. Bruce Banerdt[2]

A planet's crust bears witness to the history of planetary formation and evolution, but for Mars, no absolute measurement of crustal thickness has been available. Here, we determine the structure of the crust beneath the InSight landing site on Mars using both marsquake recordings and the ambient wavefield. By analyzing seismic phases that are reflected and converted at subsurface interfaces, we find that the observations are consistent with models with at least two and possibly three interfaces. If the second interface is the boundary of the crust, the thickness is 20 ± 5 kilometers, whereas if the third interface is the boundary, the thickness is 39 ± 8 kilometers. Global maps of gravity and topography allow extrapolation of this point measurement to the whole planet, showing that the average thickness of the martian crust lies between 24 and 72 kilometers. Independent bulk composition and geodynamic constraints show that the thicker model is consistent with the abundances of crustal heat-producing elements observed for the shallow surface, whereas the thinner model requires greater concentration at depth.

Planetary crusts form as a result of mantle differentiation and subsequent magmatic processes, including the partial melting of mantle reservoirs that may continue to the present day (*1*). For Mars, the cratering record shows that much of its crust formed early in the planet's history and was accompanied by substantial volcanism (*2*, *3*). During both the initial crystallization of a putative magma ocean as well as later-stage partial melting, incompatible components, including heat-producing elements and volatiles, concentrated in the melt and were largely sequestered into the crust. The thickness of the crust of Mars thus provides fundamental constraints on how the planet differentiated, how incompatible elements were partitioned among the major silicate reservoirs, and how the planet evolved thermally and magmatically over geologic time (*4*–*6*).

Previous estimates of the crustal thickness of Mars and its spatial variations were made by modeling the relationship between gravity and topography. By assuming Airy isostasy and using a restrictive range of crustal densities of 2700 to 3100 kg m^{-3}, the average crustal thickness of the planet was reported to be 57 ± 24 km (*7*). More recent analyses, however, have used elemental abundances of the surface (*8*) along with major element chemistry of martian meteorites to argue that the crust could be considerably denser, with values close to ~3300 kg m^{-3}. If these higher densities were representative of the underlying crust, the gravity data would allow average crustal thicknesses up to 110 km (*9*). By contrast, bulk crustal densities lower than those previously

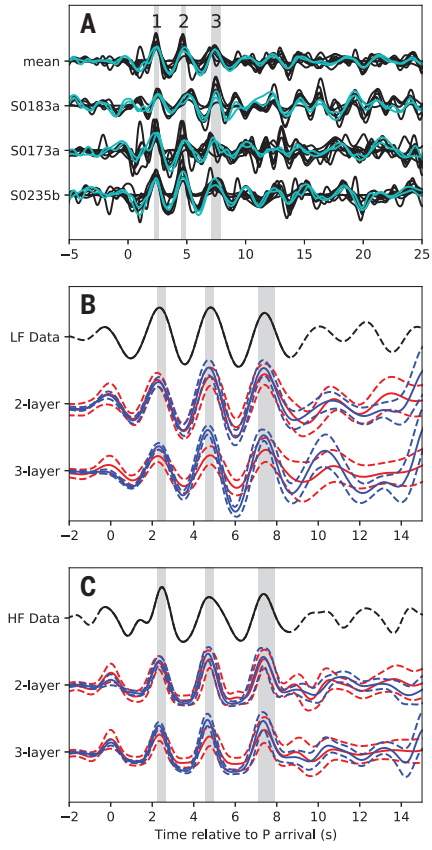

Fig. 1. Measured and modeled converted phases that constrain the crustal structure at the InSight landing site. (**A**) *P*-to-*S* receiver functions for the three events considered (S0183a, S0173a, and S0235b) and the summed trace. Different traces for each event correspond to different processing methods as described in the supplementary materials. Gray shading highlights the three clear positive phases within the first 8 s. Numbered labels correspond to predicted ray paths shown in Fig. 2, B and D. The two datasets used for model inversions shown in Fig. 2 are highlighted in cyan. (**B**) Comparison between the low-frequency (LF) representative receiver function sum trace and synthetic summed *P*-to-*S* receiver functions for the two- and three-layer models. Data are shown in black on top, with solid portion of the line representing the time window used in the inversion. Solid and dashed red lines show the synthetics computed by the range of models produced by inversion method A (*16*), whereas solid and dashed blue lines show the mean receiver functions with standard deviations based on the 5000 best-fitting receiver functions derived from inversion method B (*16*). Gray-shaded regions are the same as in (A). (**C**) Same as (B) but for the high-frequency (HF) receiver functions.

[1]Bensberg Observatory, University of Cologne, Vinzenz-Pallotti-Str. 26, 51429 Bergisch Gladbach, Germany. [2]Jet Propulsion Laboratory, California Institute of Technology, 4800 Oak Grove Dr., M/S 183-301, Pasadena, CA 91109, USA. [3]Institute of Geophysics, ETH Zurich, Sonneggstr. 5, 8092 Zürich, Switzerland. [4]Max Planck Institute for Solar System Research, Justus-von-Liebig-Weg 3, 37077 Göttingen, Germany. [5]Physik-Institut, University of Zurich, Zurich, Switzerland. [6]Department of Geology, University of Maryland, College Park, 8000 Regents Dr., College Park, MD, 20782-4211, USA. [7]Université de Lyon, Université Claude Bernard Lyon 1, Ecole Normale Supérieure de Lyon, Université Jean Monet, CNRS, Laboratoire de Géologie de Lyon, Terre, Planètes, Environnement, F-69622 Villeurbanne, France. [8]Research School of Earth Sciences, The Australian National University, Canberra, ACT 0200, Australia. [9]Université de Paris, Institut de Physique du Globe de Paris, CNRS, 1 rue Jussieu, F-75005 Paris, France. [10]Institut Supérieur de l'Aéronautique et de l'Espace SUPAERO, 10 Avenue Edouard Belin, 31400 Toulouse, France. [11]Institut de Recherche en Astrophysique et Planétologie, Université Toulouse III Paul Sabatier, CNRS, CNES, 14 Av. E. Belin, 31400 Toulouse, France. [12]Geosciences Barcelona–CSIC, Barcelona, Spain. [13]Department of Geophysics, Colorado School of Mines, 1500 Illinois St., Golden, CO 80401, USA. [14]Institute of Planetary Research, German Aerospace Center (DLR), 12489 Berlin, Germany. [15]Université Côte d'Azur, Observatoire de la Côte d'Azur, CNRS, Laboratoire Lagrange, 06304 Nice, France. [16]Lunar and Planetary Laboratory, University of Arizona, Tucson, AZ 85721, USA. [17]Sorbonne Université, Muséum National d'Histoire Naturelle, UMR CNRS 7590, Institut de Minéralogie, de Physique des Matériaux et de Cosmochimie, IMPMC, 75005 Paris, France. [18]Department of Geosciences, Stony Brook University, Stony Brook, NY 11794-2100, USA. [19]Université de Lyon, Ecole Normale Supérieure de Lyon, Université Claude Bernard Lyon 1, Université Jean Monet, CNRS, Laboratoire de Géologie de Lyon, Terre, Planètes, Environnement, F-69007 Lyon, France. [20]Institut Universitaire de France, Paris, France. [21]Center for Star and Planet Formation, GLOBE Institute, University of Copenhagen, Copenhagen, Denmark. [22]Department of Earth, Ocean and Atmospheric Sciences, University of British Columbia, Vancouver, BC V6T 1Z4, Canada. [23]Planetary Science Institute, Tucson, 1700 East Fort Lowell, Suite 106, Tucson, AZ 85719-2395, USA. [24]Royal Observatory of Belgium, Brussels, Belgium. [25]Department of Earth, Planetary, and Space Sciences, University of California, Los Angeles, CA 90095, USA.
***Corresponding author. Email: bknapmey@uni-koeln.de** †Present address: University of Vienna, Althanstrasse 14, 1090 Vienna, Austria.

assumed (~2600 kg m^{-3}) have been inferred from gravity analyses and would allow a thinner average crustal thickness (*10*). Low densities were confirmed locally for the near-surface sediments in Gale crater (*11*) as well as the pyroclastic deposit of the Medusa Fossae Formation (*12*). Low bulk crustal densities could result from either substantial porosity or the presence of buried silica- and feldspar-rich rocks (*13*). Silica-rich magmatic rocks are potentially consistent with ancient evolved lithologies identified in martian meteorite breccias (*14*).

We used data from the Seismic Experiment for Interior Structure (SEIS) on NASA's Interior Exploration using Seismic Investigations, Geodesy and Heat Transport (InSight) mission (*15*) to provide an absolute measurement of Mars' crustal thickness and layering. Our assessment of the crustal structure at the landing site is based on a combination of methods using both converted and reflected seismic phases to resolve tradeoffs between the depth of a layer and its seismic velocity (*16*). By calculating receiver functions (*17*, *18*), we extracted *P*-to-*S* conversions from the *P*-wave coda of three seismic events with the clearest *P*-wave onsets and polarizations. In addition, we applied seismic interferometric techniques by calculating autocorrelations of both ambient noise and event coda using the vertical component. Under the assumption of a diffuse wavefield, as expected in the case of noise from homogeneously distributed, uncorrelated sources as well as in the coda of high-frequency events, the correlations can be interpreted as zero-offset vertical reflection responses (*19*). By focusing on the reflected wavefield, the autocorrelations provide independent and complementary information to the receiver-function conversion-based methods that make use of the transmitted wavefield (*20*).

In a previous study (*18*), we already considered *P*-to-*S* receiver functions for two of the same events but only inverted for the properties of the interface at the base of the shallowest layer (interpreted there as a transition from fractured to unfractured basalt within the crust), causing the first converted arrival at 2.4 s. After including an additional event and applying extensive reanalysis to the data (*16*), the *P*-to-*S* receiver functions for nine different processing methods (*16*) show three consistent positive arrivals within the first 8 s but no clear and consistent negative arrivals or later phases (Fig. 1A). Because all three events are located at epicentral distances between 25° and 59° (*21*, *22*), no strong move-out of either direct arrivals or multiple reflections is expected, which impedes the unambiguous identification of multiples. The third positive arrival at 7.2 to 7.5 s could either be simply a *PpPs* multiple of the first arrival at 2.4 s (ray path 3 in Fig. 2B) or contain additional energy from a direct conversion from a third, deeper discontinuity (ray path 3 in Fig. 2D). We applied two inversion approaches to the *P*-to-*S* receiver functions (*16*), and both can match the three clear peaks with either two (Fig. 2, A and B) or three interfaces (Fig. 2, C and D). In both inversion approaches, our models showed robust and consistent depths of the two shallowest interfaces. The first layer with a thickness of 6 to 11 km and an *S*-wave velocity between 1.2 and 2.1 km s^{-1} is consistent with the previous results for the shallow crust (*18*), whereas a second interface is found at a depth of 15 to 25 km independent of the model parameterization. The third interface, the existence of which is supported but not absolutely required by the data, showed greater variability in depth between different inversion choices and generally required a smaller

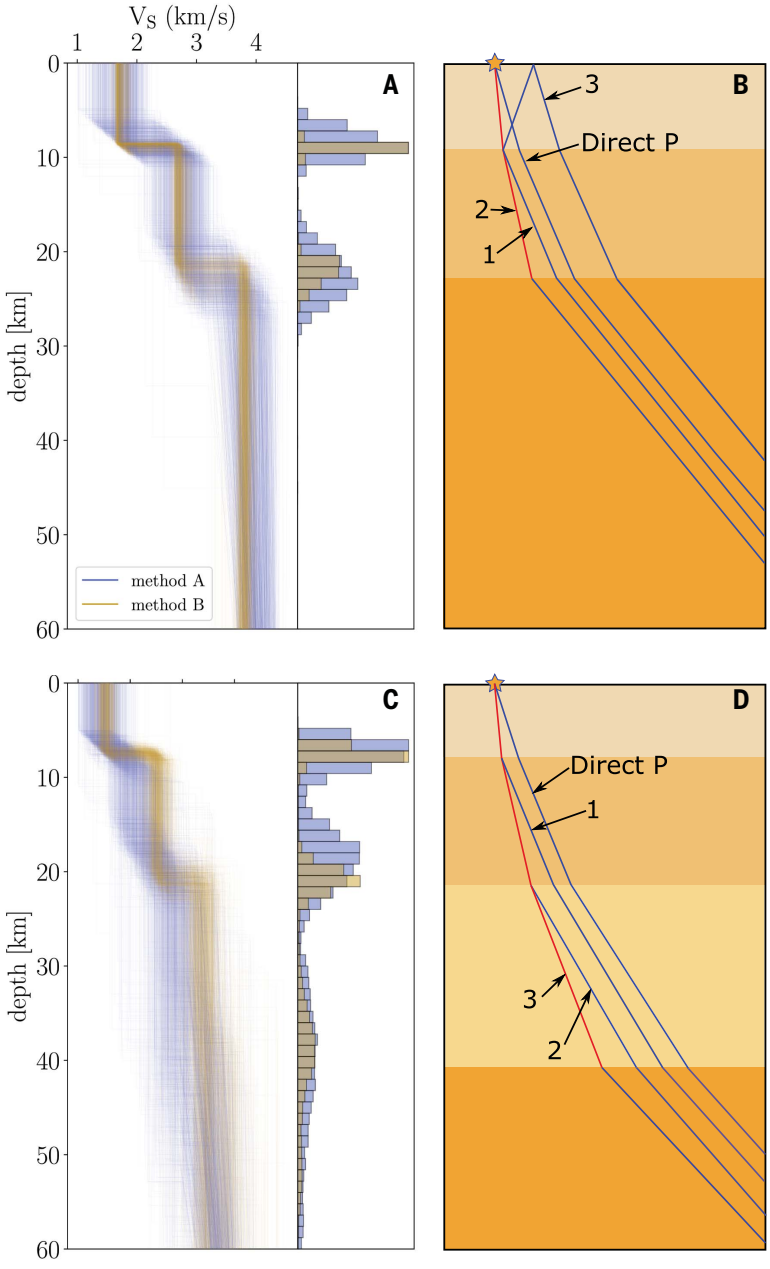

Fig. 2. Synopsis of the crustal structure of Mars at the InSight landing site from receiver-function analyses. (**A**) Inversion results for all three events using inversion method A (blue lines) and method B (brown lines) using a two-layer parameterization. (**B**) Cartoon showing the ray paths of the main direct and converted phases present in the data. Blue lines show *P*-phase paths, whereas red lines show conversions to *S* phases at the interfaces below the lander. Direct conversions and one *P* multiple are shown, and numbered labels correspond to arrivals identified in Fig. 1A. (**C** and **D**) Same as (A) and (B) except for the assumption of a three-layer model and exclusion of the multiple arrival.

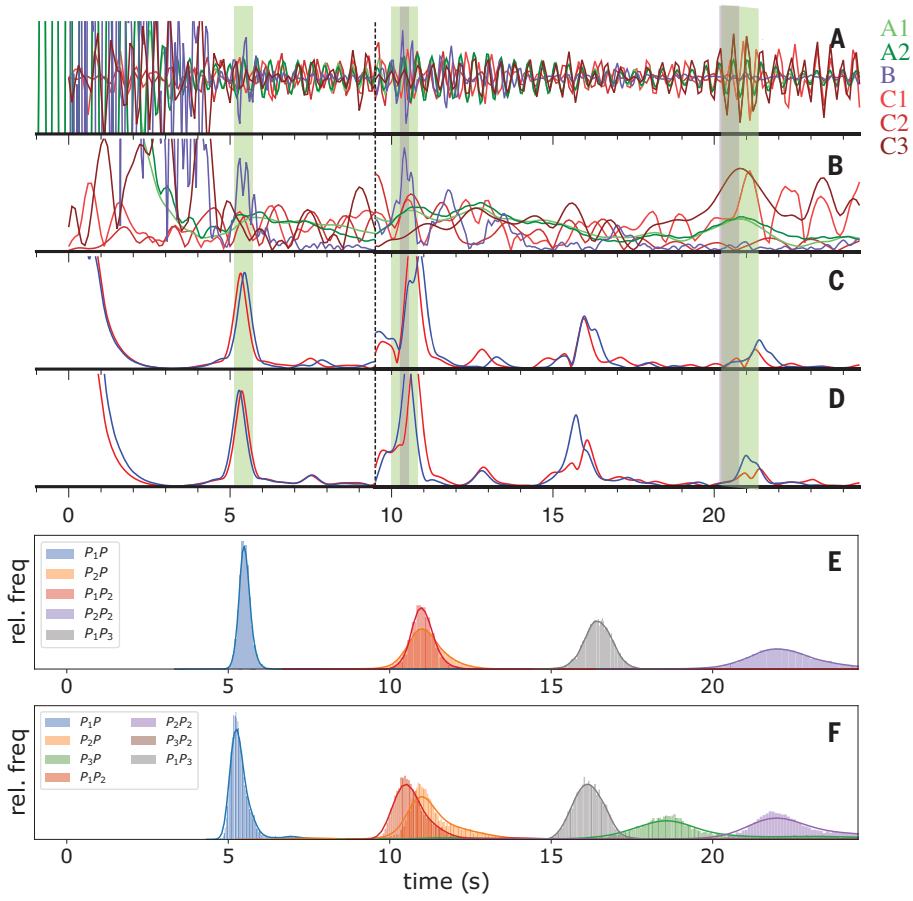

Fig. 3. Autocorrelation functions for different datasets, components, and processing methods. (**A**) Overlaid traces are from the three analysis methods discussed in the supplementary materials. The dashed bar at 9.5 s corresponds to a change in normalization in order to see smaller amplitude arrivals later in the trace. Green bars highlight areas where all methods are nearly in-phase and show potential arrivals, whereas purple bars highlight arrivals indicated from an independent study (*24*). (**B**) Envelopes of the autocorrelation functions displayed in (A). (**C**) Envelopes of synthetic zero-offset Green's functions for a representative model from the family of two-layer models in Fig. 2A for method A in blue and method B in red. (**D**) Same as (C) but for the three-layer models from Fig. 2C. (**E**) Histograms of predicted arrivals from the family of two-layer models as shown in Fig. 2A. The first subscript of the arrival in the legend refers to the interface of reflection, and the second subscript (if present) represents a second or third bounce between the free surface and that interface. rel. freq., relative frequency. (**F**) Same as (E) but for the three-layer models in Fig. 2C.

velocity contrast at the base of this layer than for the shallower second interface (figs. S18 and S19). Based on the ensemble of models from the two inversion approaches, our results are consistent with either a local crustal thickness at the InSight landing site of 15 to 25 km, when the base of layer 2 is the Moho (thin-crust models), or 27 to 47 km, when the base of layer 3 is the Moho (thick-crust models; Fig. 2 and figs. S18 and S19). *S*-to-*P* receiver functions can also be calculated for two events (S0173a and S0235b; figs. S4, S6, and S7), and both show a signal consistent with conversion at the first interface, whereas S0235b also shows possible arrivals consistent with deeper conversions (*16*). Further support for the *P*-to-*S* receiver function–derived models is provided by waveform fits in inversions for source mechanisms (*16*), where a strong interface at a depth around 24 km is required to match *S* precursors.

Vertical component autocorrelations based on different datasets and processing algorithms (*16*, *23*) show consistent energy maxima in the 5- to 6-s, 10- to 11-s, and 20- to 21.5-s time ranges (Fig. 3). Comparison with predicted arrival times from representative models produced by the receiver-function inversion shows that these energy maxima can be explained by *P*-wave reflections in those models interacting with the first two interfaces, without any clear observations requiring the third interface. Previously published autocorrelations (*24*) contain an arrival near 10 s that is consistent with our results and which can be explained as a *P*-wave reflection from the bottom of the second layer at a depth around 22 km. A second arrival reported by (*24*) near 20 s, which is also present in many of the autocorrelation functions calculated here, is consistent with a multiple reflection from that layer (Fig. 3). These arrivals were interpreted by Deng and Levander (*24*) as *P* and *S* reflections, respectively, from a crust-mantle discontinuity at a depth of 35 km. However, we do not expect a strong *S* reflection in a vertical autocorrelation because vertically propagating *S* waves are horizontally polarized. Interpreting the second arrival as a multiple *P* reflection instead is consistent with our receiver function–derived results and more likely to be observed in a vertical component autocorrelation. The previously published crustal thickness estimate of 35 km based on autocorrelations (*24*) is consistent with the possible range of the thick-crust models, but the specific arrivals identified in that study are more consistent with a reflection and multiple from the shallower second interface at a depth around 20 km.

We inverted for the thickness of the crust at a global scale using the seismically estimated thickness at the InSight landing site and the observed gravity field as constraints (*16*). Our models consider the gravity of hydrostatic relief along density interfaces beneath the lithosphere, surface relief, variations in thickness of a constant density crust, and the low-density polar cap deposits (*25*). We used several different interior prelanding models (*26*) that specify the density profile of the mantle and core, and, for each, we constructed crustal thickness models for all permissible crustal densities. For a given seismic thickness, the mean thickness of the crust depends almost exclusively on the density contrast across the crust-mantle interface (fig. S22). To ensure that the thickness of the crust is positive within the major impact basins, each reference model has a maximum permissible crustal density. If the thin-crust seismic model is used as a constraint, the global mean crustal thickness is predicted to lie between 24 and 38 km and the maximum permissible density of the crust is 2850 kg m^{-3} (Fig. 4 and figs. S22 and S23). For the thick-crust seismic model, the average crustal thickness lies between 39 and 72 km and the maximum permissible crustal density is 3100 kg m^{-3} (Fig. 4 and figs. S22 and

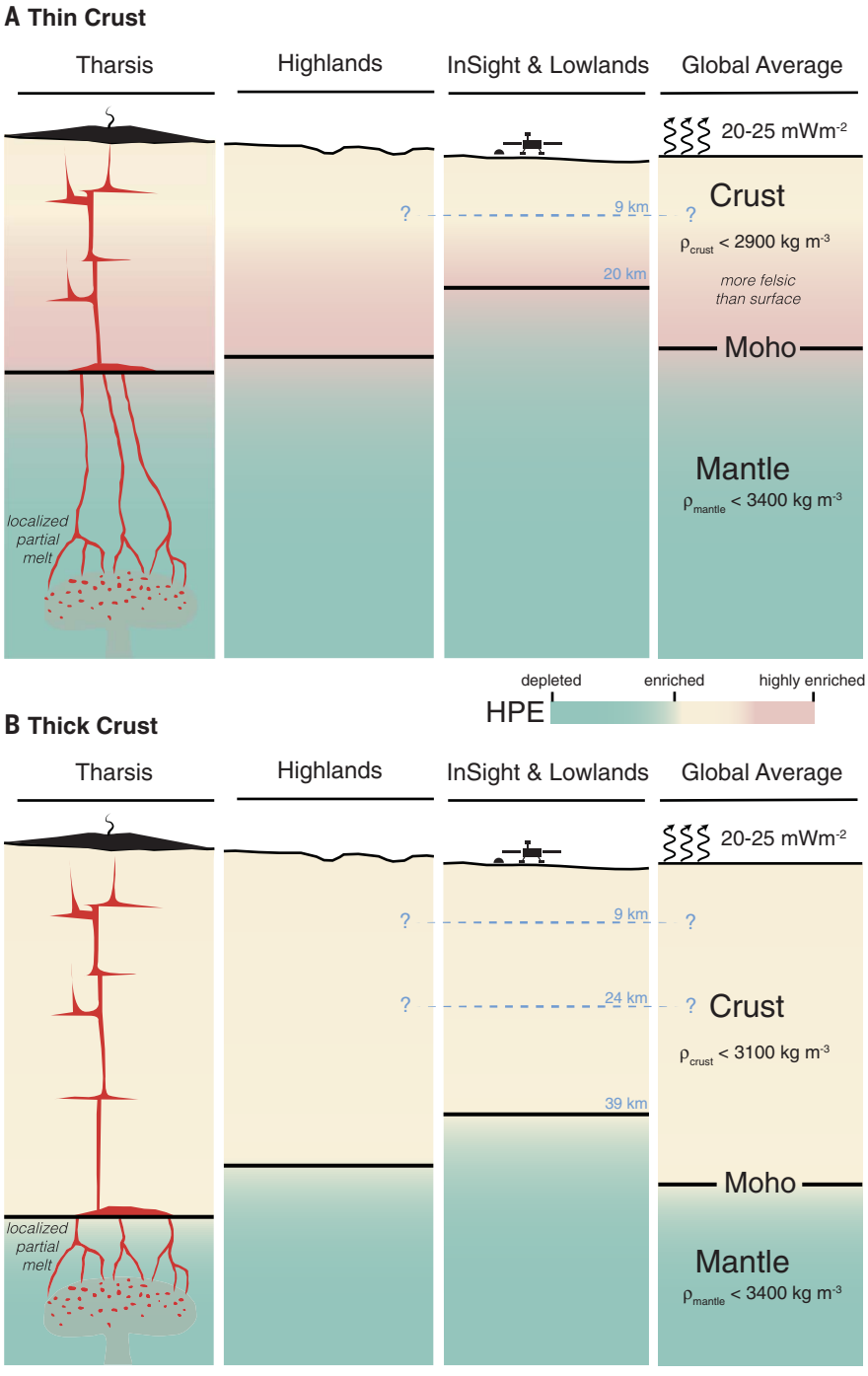

Fig. 4. Schematic interpretations of the geochemical and geodynamical implications for the thin- and thick-crust models. (**A** and **B**) To match geodynamic constraints, an enrichment of heat-producing elements (HPEs), shown in color, and lower density than observed from the surface are required in the thin-crust model (A), whereas the thick-crust model (B) is consistent with surface observations. ρ, density.

S23). For both seismic constraints, the crustal density is substantially less than would be expected based on the composition of surface materials (*9*), which is close to 3300 kg m^{-3}. The lower bulk densities are signatures of highly altered layers and can be accounted for by the presence of more than 5% porosity in the crust on average, the presence of fluids or low-density cements filling fractures and pore space, the existence of abundant petrologically evolved felsic rocks beneath the surface layer, or a combination thereof.

The seismic observations argue for a relatively thin crust, or at least thinner than some earlier predictions (*9*), providing constraints on crustal heat production and the degree of planetary silicate differentiation (Fig. 4). Because the present-day crustal thickness is the outcome of the planet's differentiation history (*27*, *28*), geodynamic and geologic modeling can place constraints on the composition of the crust and of the mantle, and on the cooling rate of the planet (*16*). Our results indicate that average crustal thickness models that are consistent with the thick-crust seismic model are compatible with currently accepted bulk (*29*, *30*) and crustal (*8*, *31*) heat-producing element contents and the occurrence of present-day melting only in an ascending plume below the thickened crust of the Tharsis province (fig. S27). Such a scenario implies a crust that is about 13 times more enriched in heat-producing elements than the primitive mantle (fig. S24), consistent with 55 to 70% of the martian heat-producing elements being sequestered into the crust. By contrast, the thin-crust seismic model requires a crust that is about 21 times more enriched than a relatively cold primitive mantle (fig. S25). This is more than two times larger than estimates from gamma-ray spectroscopy data that constrain the surface layer of the crust (table S6) and would point toward an enrichment in heat-producing elements beneath the surface layer (*16*). Furthermore, this would call for an efficient process of incompatible element extraction from the mantle, possibly by upward segregation during the solidification of a magma ocean or by a secondary differentiation mechanism, as for the continental crust of Earth. In both crustal models, assuming a Wänke and Dreibus (*29*) bulk composition, the present-day heat flux is predicted to lie between 20 and 25 mW m^{-2} (Fig. 4). The depth to the crust-mantle boundary, as well as layering in the crust, can further constrain crustal magnetization amplitudes, depending on whether the magnetization is carried in upper or lower crustal layers, or both (*16*). We can also investigate whether crustal thickness and density models are consistent with moment-of-inertia measurements and constraints on the properties of Mars core from the k_2 tidal Love number (*16*). Generally, these constraints are easier to match for most mantle composition models with the thick-crust seismic models, although some models also allow for the thin-crust model. Overall, when considering geodynamic, geochemical, and geodetic constraints, the thin-crust models place tighter constraints on the density and enrichment of heat-producing elements within the crust, as well as on the mantle composition, than the thick-crust models, but neither of the two can be excluded.

REFERENCES AND NOTES

1. L. T. Elkins-Tanton, *Annu. Rev. Earth Planet. Sci.* **40**, 113–139 (2012).
2. M. Grott *et al.*, *Space Sci. Rev.* **174**, 49–111 (2013).
3. F. Nimmo, K. Tanaka, *Annu. Rev. Earth Planet. Sci.* **33**, 133–161 (2005).

4. D. Breuer, W. B. Moore, in *Physics of Terrestrial Planets*, vol. 10 of *Treatise on Geophysics*, G. Schubert, Ed. (Elsevier, ed. 2, 2015), pp. 255–305.
5. S. A. Hauck II, R. J. Philips, *J. Geophys. Res.* **107**, 5052 (2002).
6. A.-C. Plesa *et al.*, *Geophys. Res. Lett.* **45**, 12198–12209 (2018).
7. M. A. Wieczorek, M. T. Zuber, *J. Geophys. Res.* **109**, E01009 (2004).
8. B. C. Hahn, S. M. McLennan, E. C. Klein, *Geophys. Res. Lett.* **38**, L14203 (2011).
9. D. Baratoux *et al.*, *J. Geophys. Res.* **119**, 1707–1727 (2014).
10. S. Goossens *et al.*, *Geophys. Res. Lett.* **44**, 7686–7694 (2017).
11. K. W. Lewis *et al.*, *Science* **363**, 535–537 (2019).
12. L. Ojha, K. Lewis, *J. Geophys. Res.* **123**, 1368–1379 (2018).
13. V. Sautter *et al.*, *Nat. Geosci.* **8**, 605–609 (2015).
14. M. Humayun *et al.*, *Nature* **503**, 513–516 (2013).
15. P. Lognonné *et al.*, *Space Sci. Rev.* **215**, 12 (2019).
16. Methods and additional materials are available as supplementary materials.
17. C. A. Langston, *J. Geophys. Res.* **84**, 4749–4762 (1979).
18. P. Lognonné *et al.*, *Nat. Geosci.* **13**, 213–220 (2020).
19. K. Wapenaar, D. Draganov, R. Snieder, X. Campman, A. Verdel, *Geophysics* **75**, 75A195–75A209 (2010).
20. D. Kim, V. Lekić, *Geophys. Res. Lett.* **46**, 13722–13729 (2019).
21. D. Giardini *et al.*, *Nat. Geosci.* **13**, 205–212 (2020).
22. A. Khan *et al.*, *Science* **373**, 434–438 (2021).
23. N. Compaire *et al.*, *J. Geophys. Res.* **126**, e2020JE006498 (2021).
24. S. Deng, A. Levander, *Geophys. Res. Lett.* **47**, e2020GL089630 (2020).
25. M. A. Wieczorek, M. Beuthe, A. Rivoldini, T. Van Hoolst, *J. Geophys. Res. Planets* **124**, 1410–1432 (2019).
26. S. E. Smrekar *et al.*, *Space Sci. Rev.* **215**, 3 (2019).
27. H. Samuel, P. Lognonné, M. Panning, V. Lainey, *Nature* **569**, 523–527 (2019).
28. M. Thiriet, C. Michaut, D. Breuer, A. C. Plesa, *J. Geophys. Res. Planets* **123**, 823–848 (2018).
29. H. Wänke, G. Dreibus, *Philos. Trans. R. Soc. London Ser. A* **349**, 285–293 (1994).
30. G. J. Taylor, *Geochemistry* **73**, 401–420 (2013).
31. S. R. Taylor, S. M. McLennan, *Planetary Crusts: Their Composition, Origin and Evolution* (Cambridge Univ. Press, 2009).
32. InSight Mars SEIS Data Service, SEIS raw data, InSight Mission, IPGP, JPL, CNES, ETHZ, ICL, MPS, ISAE-Supaero, LPG, MFSC. SEIS (2019); https://doi.org/10.18715/SEIS.INSIGHT.XB_2016.
33. B. Knapmeyer-Endrun *et al.*, Crustal models of Mars at the InSight landing site from InSight seismic data (2021); https://doi.org/10.18715/IPGP.2021.kqwc4yaf.

ACKNOWLEDGMENTS

This is Insight Contribution Number (ICN) 187. We acknowledge NASA, CNES, their partner agencies and institutions (UKSA, SSO, DLR, JPL, IPGP-CNRS, ETHZ, IC, and MPS-MPG), and the flight operations team at JPL, SISMOC, MSDS, IRIS-DMC, and PDS for providing SEED SEIS data. **Funding:** M.P.P., S.T., E.B., S.E.S., and W.B.B. were supported by the NASA InSight mission and funds from the Jet Propulsion Laboratory, California Institute of Technology, under a contract with NASA. F.B. was supported by research grant ETH-05 17-1. A.K., D.G., M.v.D., and S.S. acknowledge funding by the Swiss National Science Foundation and the Swiss State Secretariat for Education, Research and Innovation, and support from ETHZ through the ETH+ funding scheme (ETH+02 19-1). V.L. and D.K. acknowledge funding from a Packard Foundation Fellowship to V.L. B.T. is supported by the European Union's Horizon 2020 research and innovation program under Marie Sklodowska-Curie grant agreement 793824. French co-authors acknowledge the support of CNES and ANR (MAGIS, ANR-19-CE31-0008-08). N.S. was supported by NASA grant 80NSSC18K1628. E.B. was funded through NASA Participating Scientist Program grant 80NSSC18K1680. A.-C.P. gratefully acknowledges the financial support and endorsement from the DLR Management Board Young Research Group Leader Program and the Executive Board Member for Space Research and Technology. Geodynamical models used in this work were performed on the supercomputer ForHLR funded by the Ministry of Science, Research and the Arts Baden-Württemberg and by the Federal Ministry of Education and Research. S.M.M. was funded through NASA InSight Participating Scientist Program award no. 80NSSC18K1622. C.M. acknowledges the support of the Institut Universitaire de France (IUF). C.L.J. and A.M. acknowledge support from the InSight Mission, the Canadian Space Agency, and ETH Zurich (ETH fellowship 19-2 FEL-34). N.B. is supported by research grant ETH-06 17-02. The work of A.R. was financially supported by the Belgian PRODEX program managed by the European Space Agency in collaboration with the Belgian Federal Science Policy Office. **Author contributions:** B.K.-E., M.P.P., F.B., R.J., A.K., D.K., V.L., B.T., S.T., M.P., N.C., R.F.G., L.M., M.S., É.S., N.S., A.-C.P., M.W., D.A., S.M.M., H.S., C.M., L.P., S.E.S., C.L.J., P.L., M.K., D.G., and W.B.B. contributed to the conceptualization of this study. The applied methodologies were developed by B.K.-E., F.B., R.J., A.K., D.K., V.L., B.T., S.T., M.P., N.C., R.F.G., L.M., M.S., É.S., A.-C.P., M.W., H.S., C.M., L.P., P.M.D., P.L., B.P., and J.-R.S. B.K.-E., F.B., R.J., A.K., D.K., N.C., M.S., É.S., A.-C.P., M.W., H.S., C.M., P.M.D., P.L., B.P., and J.-R.S. developed, implemented, and tested the software that was used. B.K.-E., M.P.P., N.S., N.B., and M.v.D. provided validation. Formal analyses were conducted by B.K.-E., R.B., R.J., A.K., D.K., V.L., B.T., S.T., M.P., N.C., M.S., É.S., A.-C.P., M.W., A.B., H.S., C.M., C.L.J., N.B., A.M., A.R., P.M.D., P.L., B.P., J.-R.S., and S.S. B.K.-E., F.B., R.J., A.K., D.K., V.L., S.T., M.P., N.C., M.S., É.S., A.-C.P., M.W., S.M.M., H.S., C.M., C.L.J., N.B., A.M., A.R., P.M.D., P.L., B.P., J.-R.S., and S.S. provided investigations. Data curation activities were done by P.L., S.S., M.v.D., and D.G. B.K.-E., M.P.P., F.B., R.J., A.K., D.K., V.L., B.T., S.T., N.C., R.F.G., L.M., M.S., É.S., A.-C.P., M.W., S.M.M., H.S., C.M., C.L.J., N.B., A.M., A.R., and P.M.D. contributed to the writing of the original draft. Review and editing were performed by B.K.-E., M.P.P., N.S., E.B., A.B., D.A., S.E.S., C.L.J., and M.K. B.K.-E., M.P.P., F.B., R.J., A.K., D.K., V.L., B.T., N.C., M.S., É.S., N.S., A.-C.P., M.W., H.S., C.M., A.M., A.R., and P.M.D. worked on visualizing the results. B.K.-E., M.P.P., A.K., R.F.G., L.M., N.S., C.L.J., P.L., and D.G. supervised junior scientists involved in the project. The InSight mission is managed by W.B.B., M.P.P., and S.E.S. The SEIS instrument development was led by P.L., D.G., and W.B.B. **Competing interests:** The authors declare no competing interests. **Data and materials availability:** All InSight SEIS data (*32*) used in this paper are available from the IPGP Data Center, IRIS-DMC, and NASA PDS. Crustal models derived in this study (Fig. 2) are available from MSDS (*33*).

SUPPLEMENTARY MATERIALS

science.sciencemag.org/content/373/6553/438/suppl/DC1
Materials and Methods
Figs. S1 to S29
Tables S1 to S6
References (*34*–*118*)

26 November 2020; accepted 21 May 2021
10.1126/science.abf8966

Thickness and structure of the martian crust from InSight seismic data

Brigitte Knapmeyer-Endrun, Mark P. Panning, Felix Bissig, Rakshit Joshi, Amir Khan, Doyeon Kim, Vedran Lekic, Benoit Tauzin, Saikiran Tharimena, Matthieu Plasman, Nicolas Compaire, Raphael F. Garcia, Ludovic Margerin, Martin Schimmel, Éléonore Stutzmann, Nicholas Schmerr, Ebru Bozdag, Ana-Catalina Plesa, Mark A. Wieczorek, Adrien Broquet, Daniele Antonangeli, Scott M. McLennan, Henri Samuel, Chloé Michaut, Lu Pan, Suzanne E. Smrekar, Catherine L. Johnson, Nienke Brinkman, Anna Mittelholz, Attilio Rivoldini, Paul M. Davis, Philippe Lognonné, Baptiste Pinot, John-Robert Scholz, Simon Stähler, Martin Knapmeyer, Martin van Driel, Domenico Giardini and W. Bruce Banerdt

Science **373** (6553), 438-443.
DOI: 10.1126/science.abf8966

Single seismometer structure

Because of the lack of direct seismic observations, the interior structure of Mars has been a mystery. Khan *et al.*, Knapmeyer-Endrun *et al.*, and Stähler *et al.* used recently detected marsquakes from the seismometer deployed during the InSight mission to map the interior of Mars (see the Perspective by Cottaar and Koelemeijer). Mars likely has a 24- to 72-kilometer-thick crust with a very deep lithosphere close to 500 kilometers. Similar to the Earth, a low-velocity layer probably exists beneath the lithosphere. The crust of Mars is likely highly enriched in radioactive elements that help to heat this layer at the expense of the interior. The core of Mars is liquid and large, ~1830 kilometers, which means that the mantle has only one rocky layer rather than two like the Earth has. These results provide a preliminary structure of Mars that helps to constrain the different theories explaining the chemistry and internal dynamics of the planet.

Science, abf2966, abf8966, abi7730, this issue p. 434, p. 438, p. 443 see also abj8914, p. 388